Supplementary Information

Accounting for Microbial–DOC Feedbacks Reveal Ecological Constraints on Artificial Upwelling for Atmospheric Carbon Dioxide Removal

Benjamin Owusu[1], Lennard Montag[1], Takasumi Kurahashi-Nakamura[1], Wolfgang Koeve[2], Sinikka T. Lennartz[1]

[1]Institute for Chemistry and Biology of the Marine Environment (ICBM), Carl von Ossietzky University Oldenburg, Germany

[2]GEOMAR Helmholtz Centre for Ocean Research Kiel, Kiel, Germany

October 16, 2026

1 The University of Victoria Earth System Climate Model (UVic-ESCM version 2.10)

The University of Victoria Earth System Climate Model (UVic ESCM) version 2.10 (Figure S1) is an Earth System Model of Intermediate Complexity (Weaver et al., 2001). The model couples ocean, sea ice, atmosphere, and terrestrial components on a common horizontal grid of 3.6 ° longitude by 1.8 ° latitude. The ocean component, based on the Modular Ocean Model version 2 (MOM2), resolves 19 vertical layers with thickness increasing from 50 m near the surface to 590 m in the deep ocean. It includes parameterizations for isopycnal and diapycnal mixing, as well as eddy-induced tracer advection (Gent and Mcwilliams, 1990). The sea-ice module is a thermodynamic–dynamic model with elastic–visco-plastic rheology (Bitz et al., 2001; Hunke and Dukowicz, 1997), and the atmosphere is represented by a two-dimensional energy–moisture balance model (Fanning and Weaver, 1996). Monthly climatological winds from NCAR/NCEP reanalysis data (Eby et al., 2013) are prescribed to compute surface fluxes of momentum, heat, and moisture. The ocean biogeochemistry module (Keller et al., 2012) simulates phosphate, nitrate, oxygen, dissolved inorganic carbon (DIC), alkalinity (ALK), particulate detritus, and two phytoplankton functional types (ordinary phytoplankton and diazotrophs) along with zooplankton as prognostic tracers. Organic matter production and remineralisation affect nutrients, oxygen, DIC, and ALK following fixed stoichiometric ratios. Air–sea gas exchange is parameterized following (Orr

et al., 1999), and a diagnostic calcium carbonate cycle influences DIC and ALK distributions (Schmittner et al., 2008). Iron limitation is represented via a spatially prescribed iron mask adapted from the BLING model (Galbraith et al., 2010) (see Figure S2). The UVic 2.10 includes improved representations of phytoplankton light limitation, zooplankton grazing, and iron limitation, as well as a tidally induced diapycnal mixing scheme over rough topography (Simmons et al., 2004). The air–sea gas transfer parameterization was updated following OCMIP recommendations (Wanninkhof, 2014), and the stoichiometric formulation of (Paulmier et al., 2009) is applied to consistently represent the effects of nitrogen fixation and denitrification on alkalinity and oxygen.

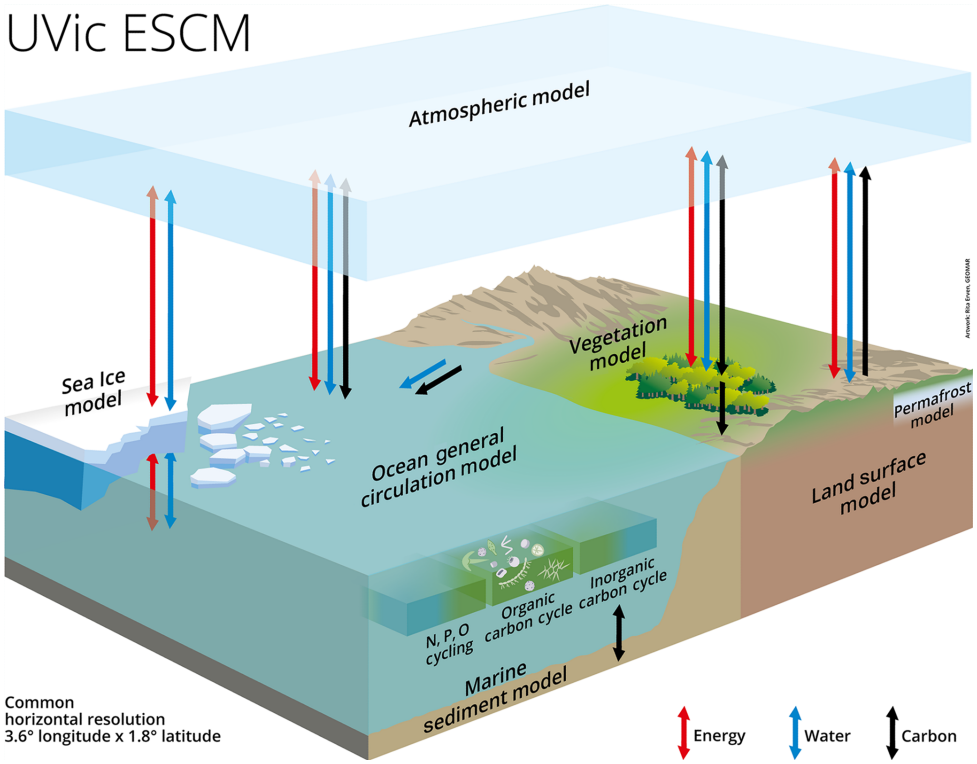


Figure S1: Schematic of the University of Victoria Earth System Climate Model version 2.10 (UVic ESCM 2.10) (Mengis et al., 2020)

1.1 Global distribution of iron limitation in UVic. Framework

The spatial distribution of the surface iron limitation factor (Figure S2) based on the prescribed iron mask in Galbraith et al. (2010) shows strong regional contrasts in iron limitation with values below 0.4 in the high-nutrient, low-chlorophyll (HNLC) regions of the Southern Ocean and the equatorial Pacific, indicating severe iron stress on phytoplankton growth. In contrast, coastal and subtropical regions exhibit weaker limitation, reflecting conditions close to iron saturation. These gradients imply that the potential for phytoplankton and microbial growth enhancement under artificial upwelling is greatest in regions currently subject to strong iron limitation. By relaxing this constraint, phytoplankton can gain a relative growth advantage which can shift the balance of carbon cycling toward increased DOC production or degradation in surface waters.

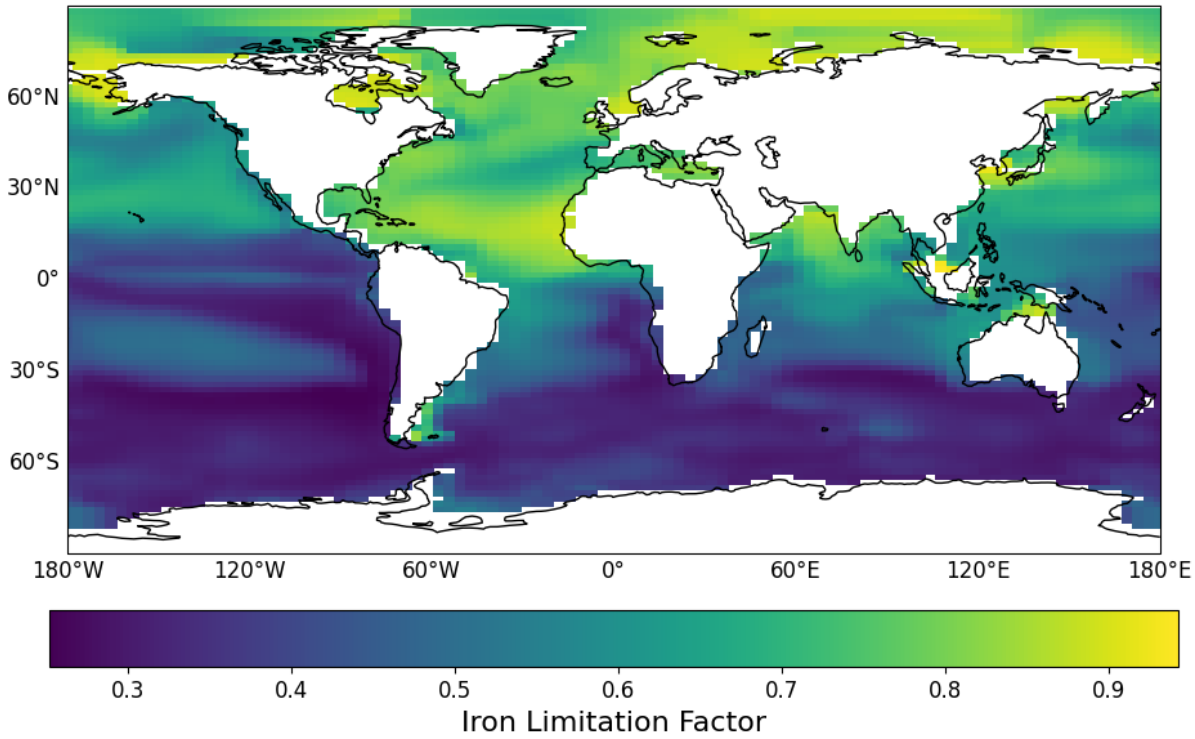


Figure S2: Global distribution of the surface (upper 35 m) iron limitation factor from Galbraith et al. (2010) data. Values range from $\sim$ 0.3 in the high-nutrient, low-chlorophyll (HNLC) regions of the Southern Ocean and equatorial Pacific to $>$ 0.9 in most coastal and subtropical regions. Lower values indicate stronger iron limitation, while higher values correspond to near-saturated iron conditions.

1.2 Global distribution of model tracer compared to observations

1.2.1 Surface nitrate distribution from model output and observations

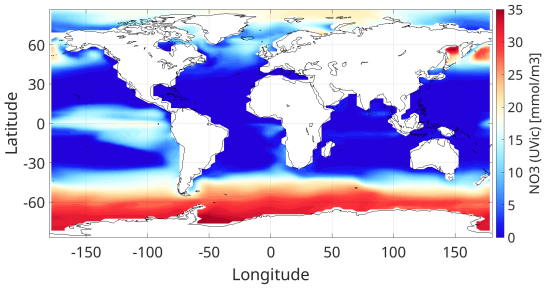


Figure S3: Global horizontal distribution of surface (50 m) NO_3 from model spin up output before simulation under AU.

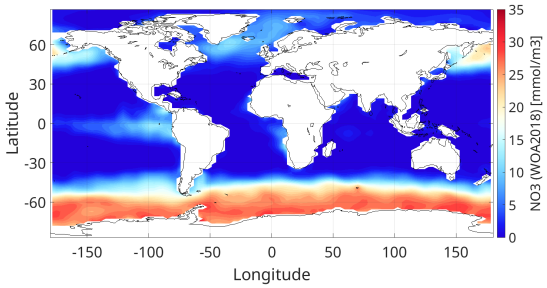


Figure S4: Global horizontal distribution of surface (50 m) NO_3 from observational data from World Ocean Atlas 2018 (Garcia et al., 2019).

1.2.2 Surface phosphate distribution from model output and observations

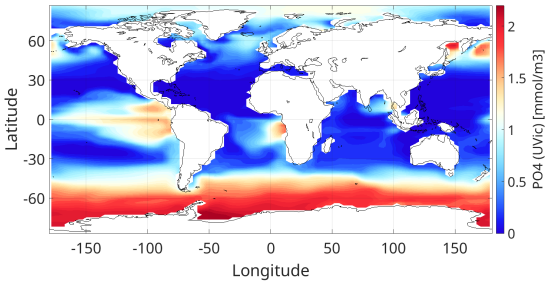


Figure S5: Global horizontal distribution of surface (50 m) PO_4 from model spin up output before simulation under AU.

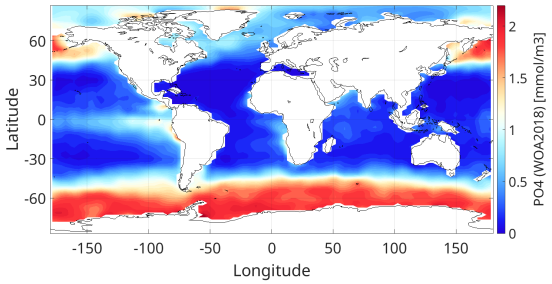


Figure S6: Global horizontal distribution of surface (50 m) PO_4 from observational data from World Ocean Atlas 2018 (Garcia et al., 2019).

1.2.3 Surface temperature distribution from model output and observations

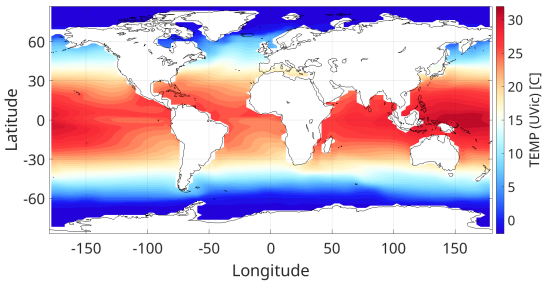


Figure S7: Global horizontal distribution of surface (50 m) temperature from model spin up output before simulation under AU.

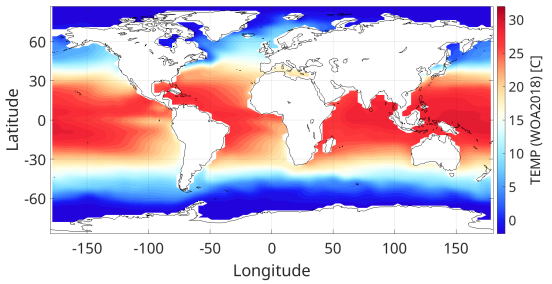


Figure S8: Global horizontal distribution of surface (50 m) temperature from observational data from World Ocean Atlas 2018 (Locarnini et al., 2018).

2 Artificial Upwelling simulation

The artificial upwelling (AU) configuration used in this study follows the approach of previous UVic model implementations (Oschlies et al., 2010; Keller et al., 2014), to simulate AU effects on the ocean and atmosphere, key tracers such as nutrients, temperature, DIC, and others are advected adiabatically from the source depth (i.e., bottom of the pipe) to the surface. The upwelling pipes extend to a maximum depth of 1000 m, with an assumed vertical velocity of 1 cm day^{-1}, averaged over the grid cell area, while a compensating downwelling flux across intermediate layers ensures volume conservation. All prognostic tracers relevant to ocean stratification and the carbon cycle (e.g., temperature, DIC, alkalinity, phosphate, nitrate, and oxygen) are included in the AU flux calculation. Since the model does not explicitly simulate an iron cycle, we adopt the simplified assumption of Keller et al. (2014), where AU relaxes surface iron limitation (limitation factor = 1) in regions where pipes are deployed. Other limiting factors, such as light availability, remain unaffected. This represents an optimistic upper-bound scenario, as dissolved iron in the ocean interior is regulated by scavenging onto organic and inorganic particles, typically resulting in

high nutrient-to-iron ratios (Tagliabue et al., 2017). The AU deployment is dynamically determined at each model time step by an algorithm designed to maximize additional oceanic carbon uptake, based on several environmental criteria. First, pipes are not activated in regions where surface phosphate concentrations exceed 0.4 mmol m^{-3}, under the assumption that such areas are not macronutrient-limited and would not benefit from nutrient enrichment. Second, pipes remain inactive where upwelling is projected to cause short-term CO_2 out-gassing to the atmosphere. This projection is based on the vertical distributions of key tracers and atmospheric pCO_2, without accounting for horizontal transport processes. For each potential source depth (model levels between 2–8), the algorithm estimates seawater $pCO_2(k)$ from temperature, salinity, alkalinity, DIC, and the vertical phosphate gradient ($\Delta PO_4 \times$ rC:P), assuming complete nutrient utilization at surface. The pipe depth selected corresponds to the level with the maximum positive difference between surface pCO_2 and $pCO_2(k)$, representing the greatest potential carbon drawdown. If this difference is negative, pipes are deactivated. The global distribution of AU coverage and pipe depths at the end of the simulation are shown in Figures S9.

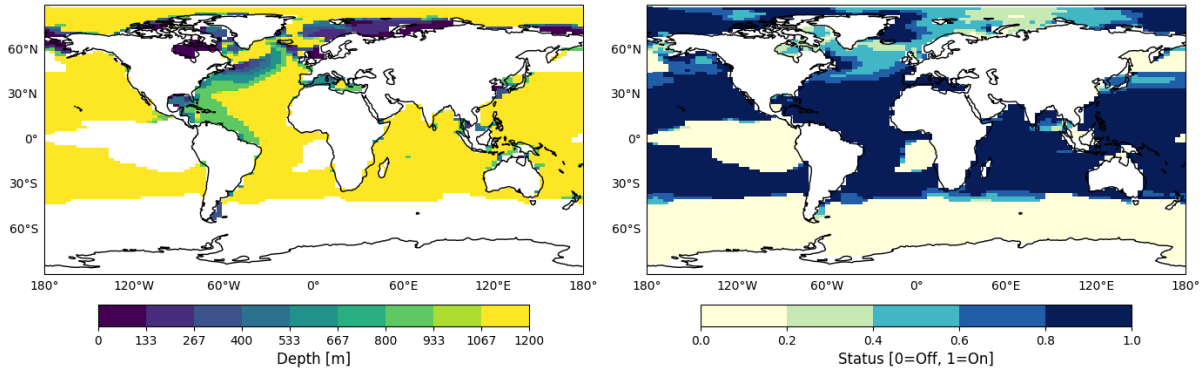


Figure S9: Spatial distribution of artificial upwelling pipes in the model domain. (Left) Pipe depth [m] showing the installation depth at the end of the simulation (Year 2110) and (Right) pipe status at the end of the simulation (Year 2110), where 1 indicates an active pipe (pipe on) and 0 indicates inactive (pipe off)

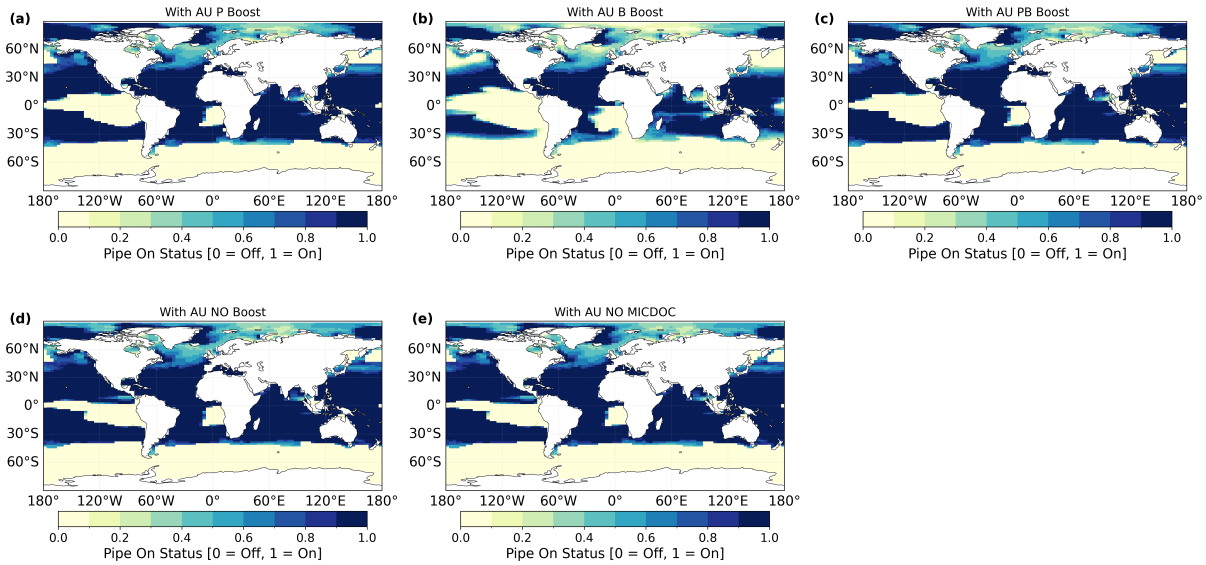


Figure S10: Global distribution of pipe status of model simulation at the end of the 100-year simulation across model variants with artificial upwelling. Each panel shows the spatial pattern of the pipe activation field, where 1 indicate that the pipe mechanism is switched on and 0 indicate it is switched off. Panel (a) AU P-Boost, (b) AU B-Boost, (c) AU PB-Boost, (d) AU NO-Boost, and (e) AU for model simulation without MICDOC. Differences among the panels illustrate how alternative model parameterization influence the spatial activation of the pipe mechanism under identical boundary conditions.

3 Spatial distribution of ocean carbon uptake

Figure S11 shows the spatial distribution of air–sea CO_2 flux anomalies between MICDOC and NO-MICDOC simulations under artificial upwelling (AU) and natural upwelling (NO-AU) conditions. Positive anomalies indicate stronger oceanic CO_2 uptake. Under AU forcing, enhanced CO_2 uptake in the MICDOC simulations (P-Boost and PB-Boost) is concentrated along upwelling margins and equatorial regions, particularly in the eastern equatorial Pacific, the western Indian Ocean, and the Atlantic sector, where artificial upwelling pipes are deployed (see Figure S9, b for pipe active regions). In contrast, the subtropical gyres exhibit weaker or negative anomalies, reflecting enhanced DOC remineralisation that offsets gains in carbon uptake. The Southern Ocean, where AU is largely absent, shows comparatively uniform fluxes, indicating that differences there stem primarily from natural upwelling and background microbial dynamics rather than direct AU forcing. Across all scenarios, AU consistently enhances regional CO_2 uptake, but the magnitude and persistence of this uptake depend on the balance between phytoplankton productivity and bacterial DOC turnover. In the P-Boost scenario, relief of phytoplankton iron limitation leads to the highest CO_2 uptake, with a substantial portion of the additional fixed carbon is temporarily retained as surface DOC. The PB-Boost case lies between these extremes, combining strong CO_2 drawdown with minimal net DOC accumulation. Taken together, the spatial anomalies in Figure S11 demonstrate that while artificial upwelling promotes CO_2 uptake globally, its long-term efficacy as a marine carbon dioxide removal (mCDR) approach is regionally modulated by microbial DOC cycling. Areas with strong iron limitation and active upwelling, such as the equatorial Pacific and Indian Ocean,

are most sensitive to these microbial feedbacks, which determine whether additional carbon is retained as DOC or rapidly remineralized back to CO_2.

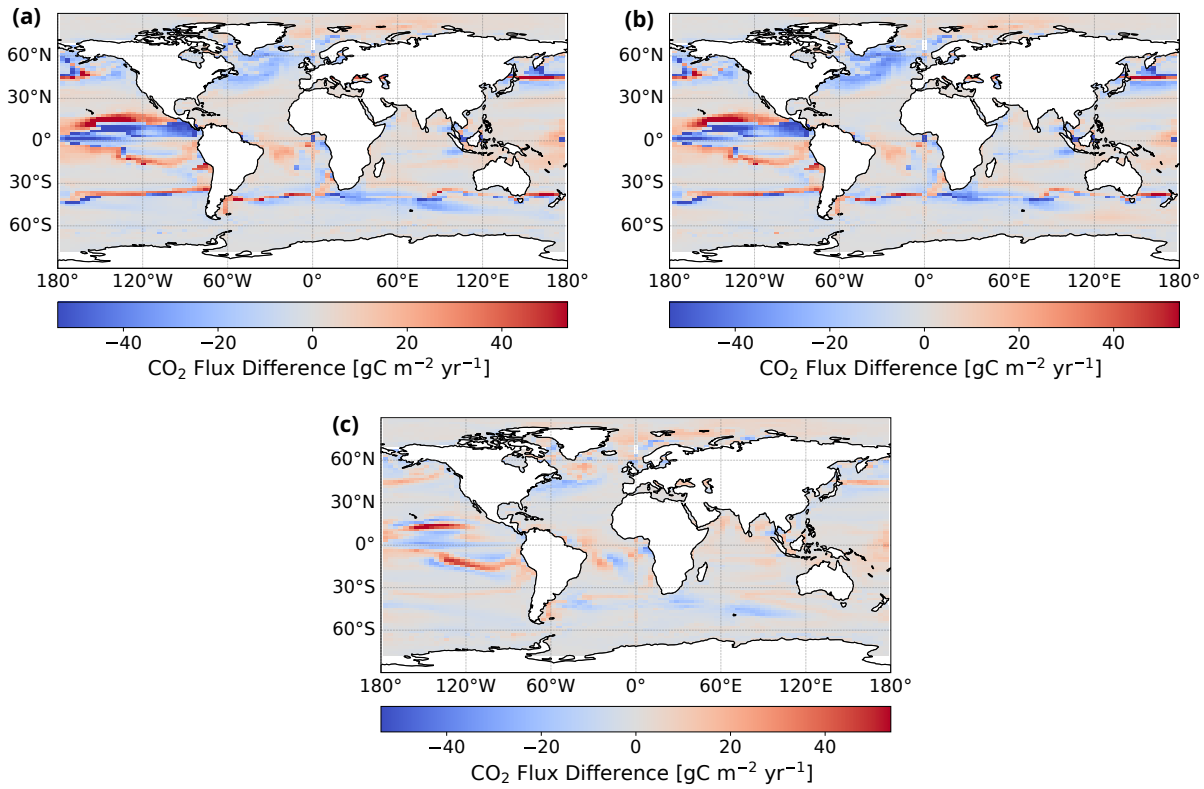


Figure S11: Spatial anomalies in air–sea CO_2 flux (gC m^{-2} yr^{-1}) between simulations with microbial–DOC feedbacks (MICDOC) and without microbial–DOC feedbacks (NO-MICDOC). The anomaly is calculated as $\Delta F_{CO_2} = F_{\mathrm{MICDOC}} - F_{\mathrm{NO-MICDOC}}$, with positive flux directed into the ocean. Positive anomalies therefore indicate enhanced oceanic CO_2 uptake in MICDOC relative to NO-MICDOC, whereas negative anomalies indicate reduced uptake. Panels (a) and (b) show anomalies under artificial upwelling for P-Boost and PB-Boost, respectively, while panel (c) shows anomalies under no-AU conditions.

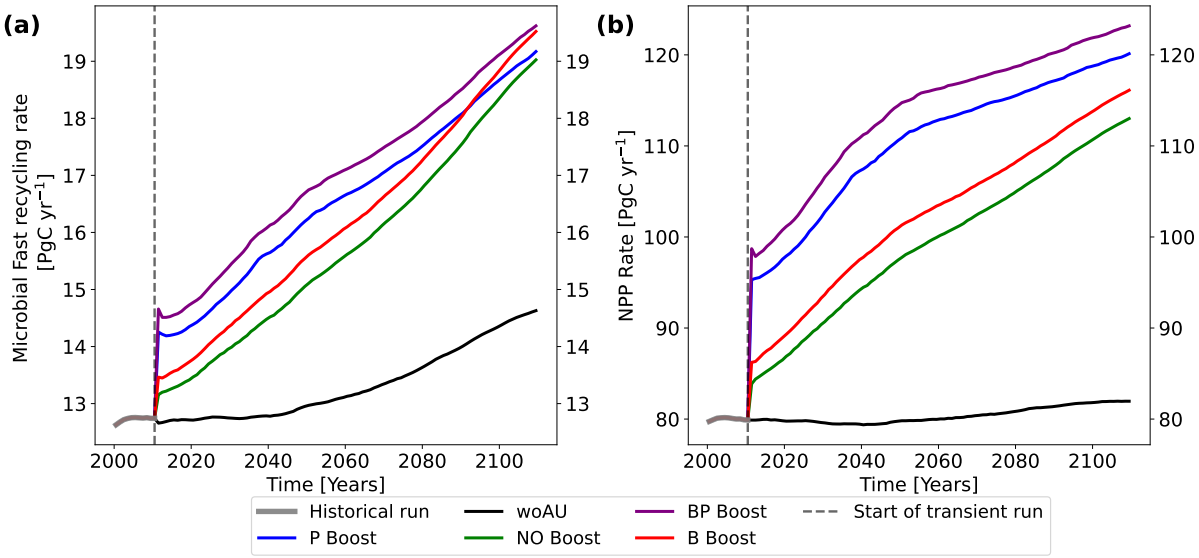


Figure S12: Time series of (a) Microbial fast recycling rate, (b) DOC production rate across the different model simulations as shown in the legend. The gray vertical dashed line shows the start of the transient simulation where AU is switched on while the gray solid trajectory shows the historical simulation for the last 20 years before the onset of AU.

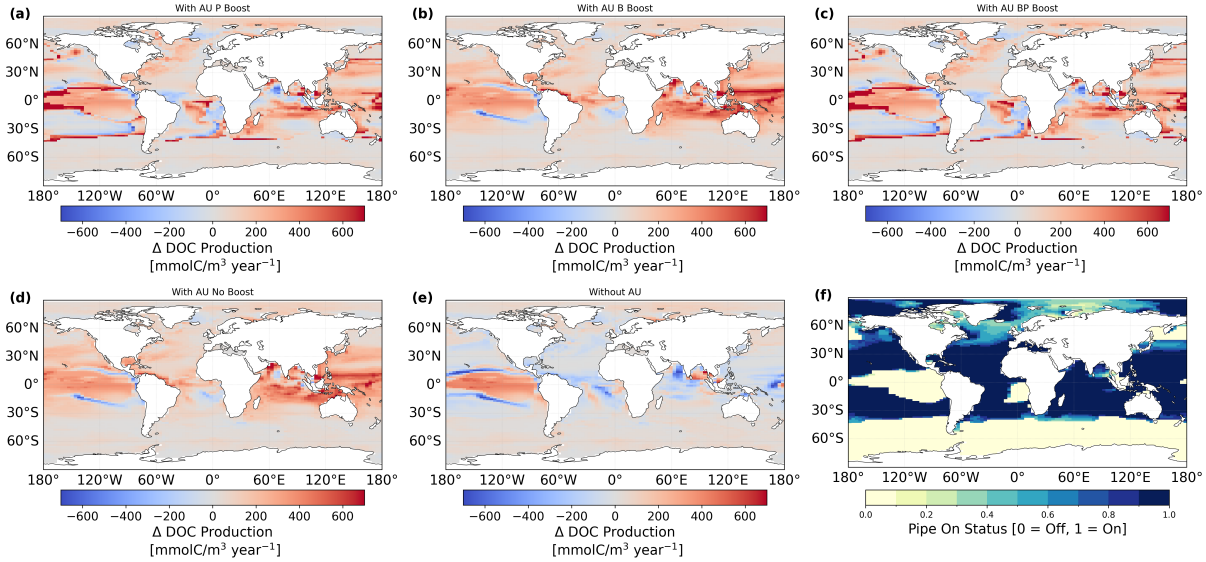


Figure S13: Global horizontal anomalies in surface (upper 50 m) DOC production [2100-2010] across model simulations: (a) P-Boost, (b) B-Boost, (c) PB-Boost, (d) NO-Boost, (e) woAU MICDOC, and (f) the status of the pipe at the end of the simulation period.

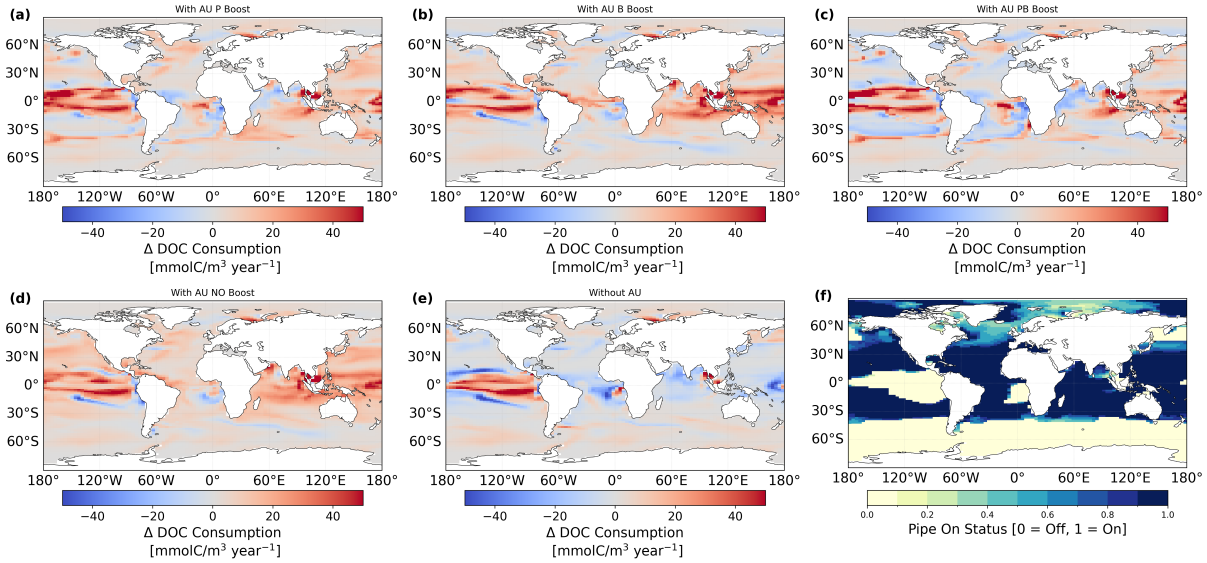


Figure S14: Global horizontal anomalies in surface (upper 50 m) DOC uptake [2100-2010] across model simulations: (a) P-Boost, (b) B-Boost, (c) PB-Boost, (d) NO-Boost, (e) woAU MICDOC, and (f) the status of the pipe at the end of the simulation period.

Table S1: Surface and global carbon inventories, biological organic carbon components, surface nutrient inventories, atmospheric CO_2, and surface ocean pCO_2 at the end of the 100-year simulation (year 2110) across the MICDOC model configurations.

Variable	Unit	Without AU	P-Boost	B-Boost	PB-Boost	NO-Boost
Surface carbon						
DOC	Pg C	15.61	17.29	12.79	14.87	14.57
DIC	Pg C	462.89	462.30	463.74	462.05	464.10
Biological organic carbon						
Phytoplankton	Pg C	0.55	0.72	0.72	0.73	0.70
Diazotrophs	Pg C	0.03	0.05	0.03	0.05	0.04
Bacteria	Pg C	0.08	0.10	0.11	0.11	0.11
Zooplankton	Pg C	0.35	0.46	0.46	0.47	0.45
Detritus	Pg C	0.10	0.15	0.14	0.15	0.14
Surface nutrients						
Nitrate	Pg N	7.29	7.52	8.21	7.40	8.26
Phosphate	Pg P	0.84	0.84	1.04	0.84	1.05
Global carbon						
DIC	Pg C	37594.25	37660.73	37610.25	37660.58	37610.24
DOC	Pg C	712.53	726.46	690.60	706.96	704.48
Atmospheric and surface CO_2						
Atmospheric CO_2	Pg C	1135.42	1072.02	1105.13	1067.75	1098.62
Surface pCO_2	model units	1059.06	989.13	1037.03	999.49	1029.26

4 Vertical profile of DOC across all MICDOC model versions

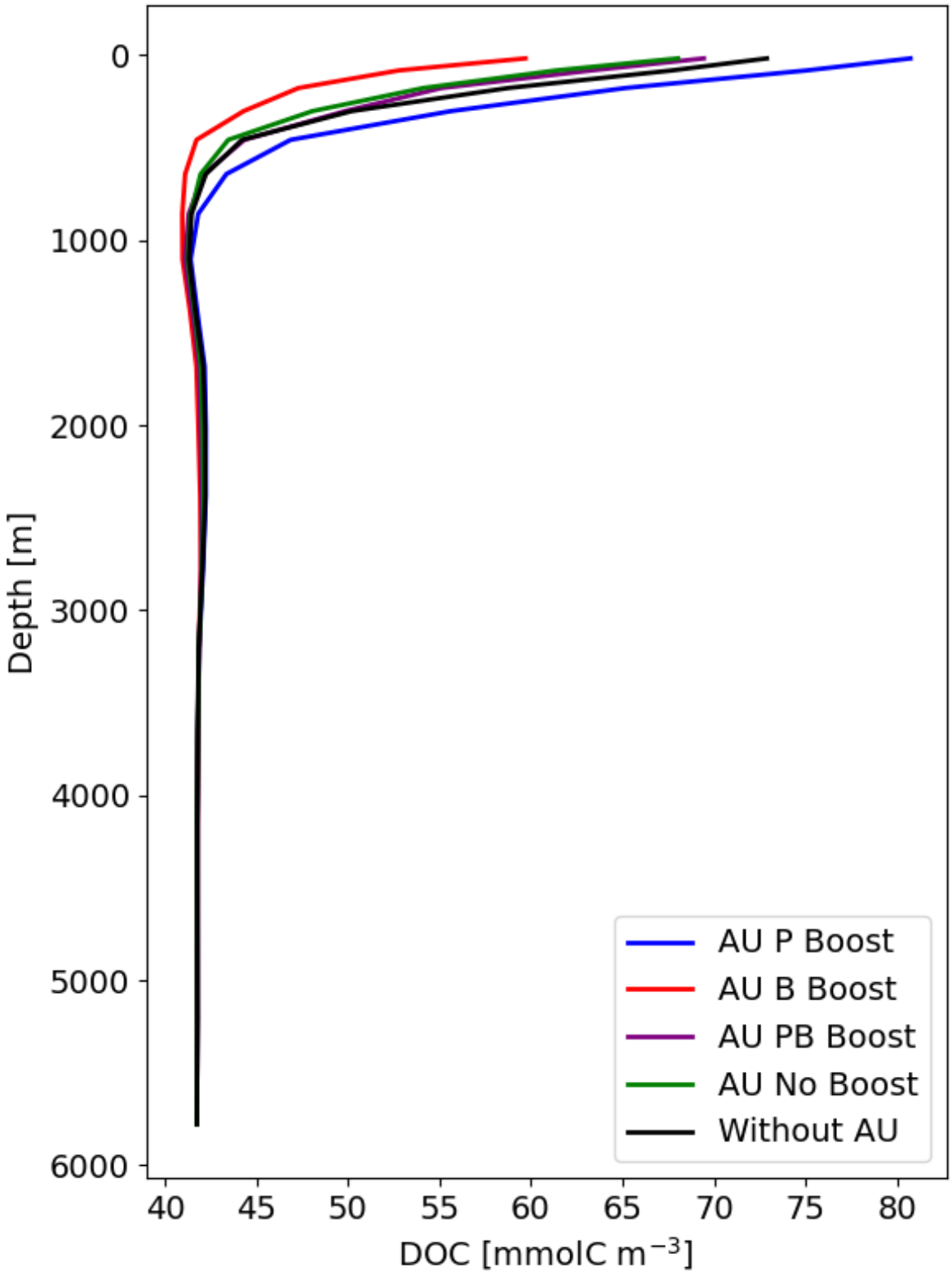


Figure S15: Vertical DOC profile across MICDOC model versions with and without AU.

DIC Transect through Pacific and Atlantic

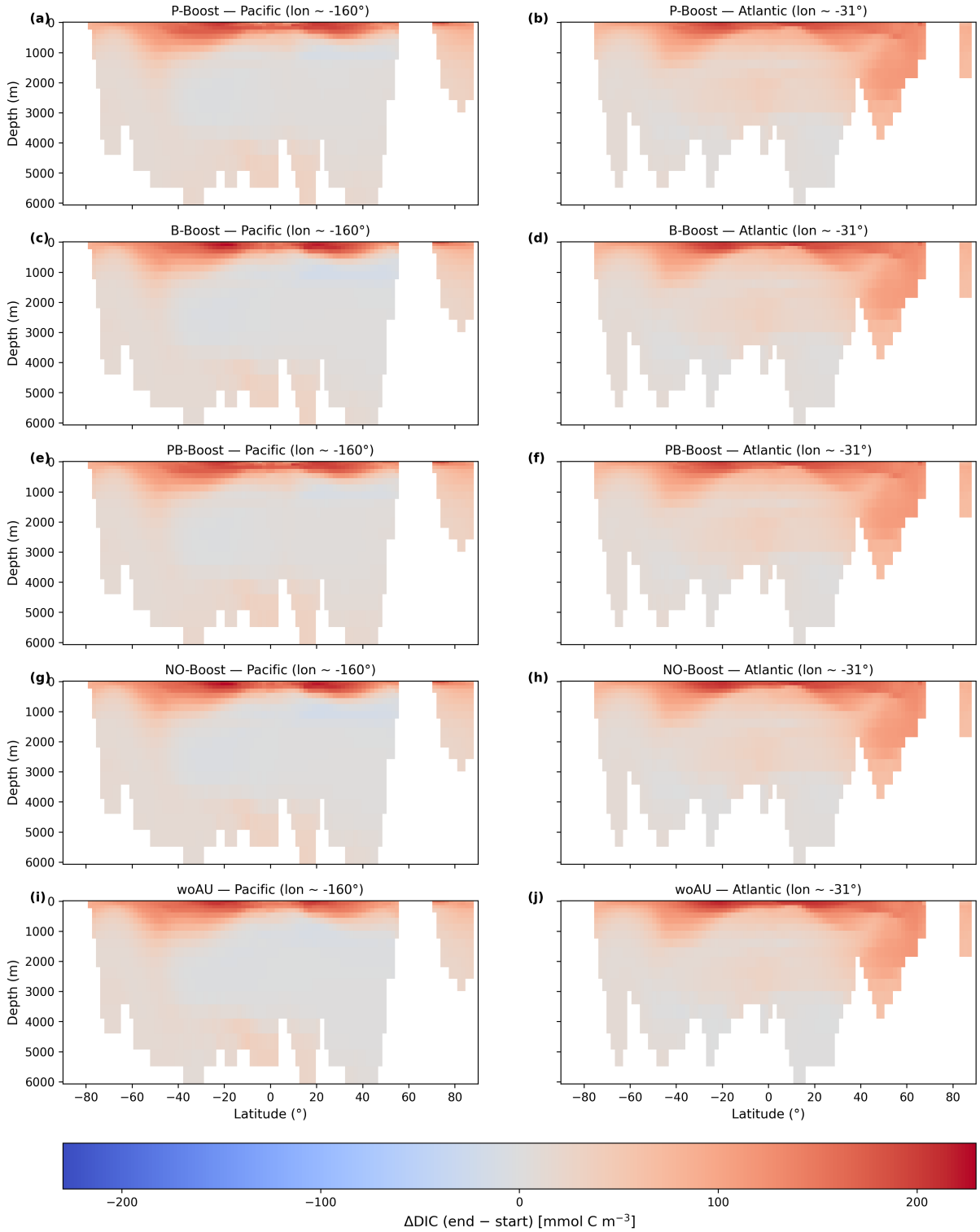


Figure S16: Meridional transects of dissolved inorganic carbon (DIC) anomalies for all simulations, showing the change between the end and the beginning of the experiment ($\Delta\text{DIC} = \text{DIC}_{end} - \text{DIC}_{start}$). Rows lettered (a-j) correspond to the different model configurations (P-Boost, B-Boost, PB-Boost, NO-Boost, and control without artificial upwelling), while columns show sections through the Pacific (∼160°W) and Atlantic (∼30°W) basins. Values are plotted in mmol C m^{-3} and represent surface-to-depth DIC concentration changes over the full 100-year integration.

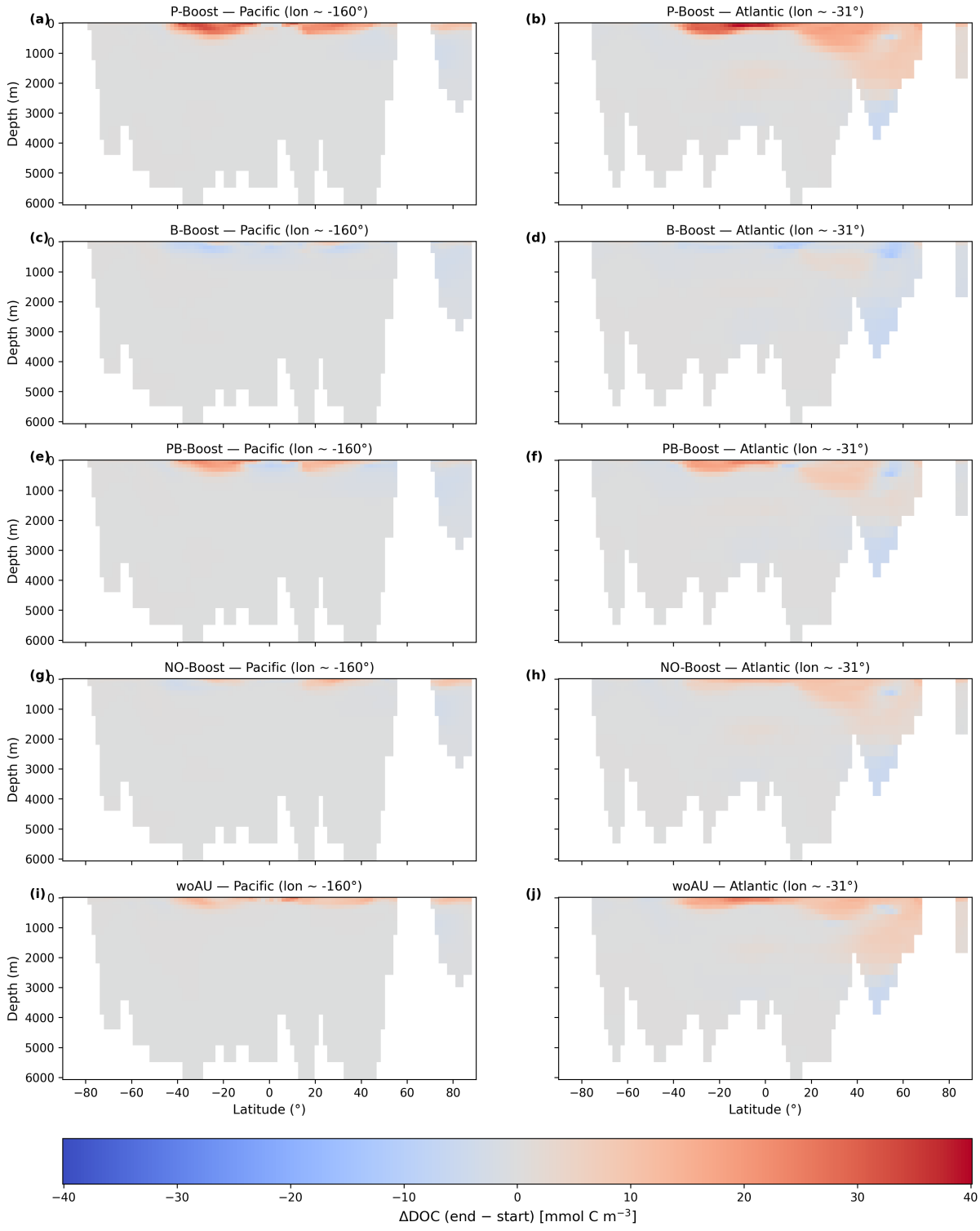


Figure S17: Meridional transects of dissolved organic carbon (DOC) anomalies for all simulations, showing the change between the end and the beginning of the experiment ($\Delta\text{DOC} = \text{DOC}_{end} - \text{DOC}_{start}$). Rows lettered (a-j) correspond to the different model configurations (P-Boost, B-Boost, PB-Boost, NO-Boost, and control without artificial upwelling), while columns show sections through the Pacific (∼160°W) and Atlantic (∼30°W) basins. Values are plotted in mmol C m^{-3} and represent surface-to-depth DOC concentration changes over the full 100-year integration.

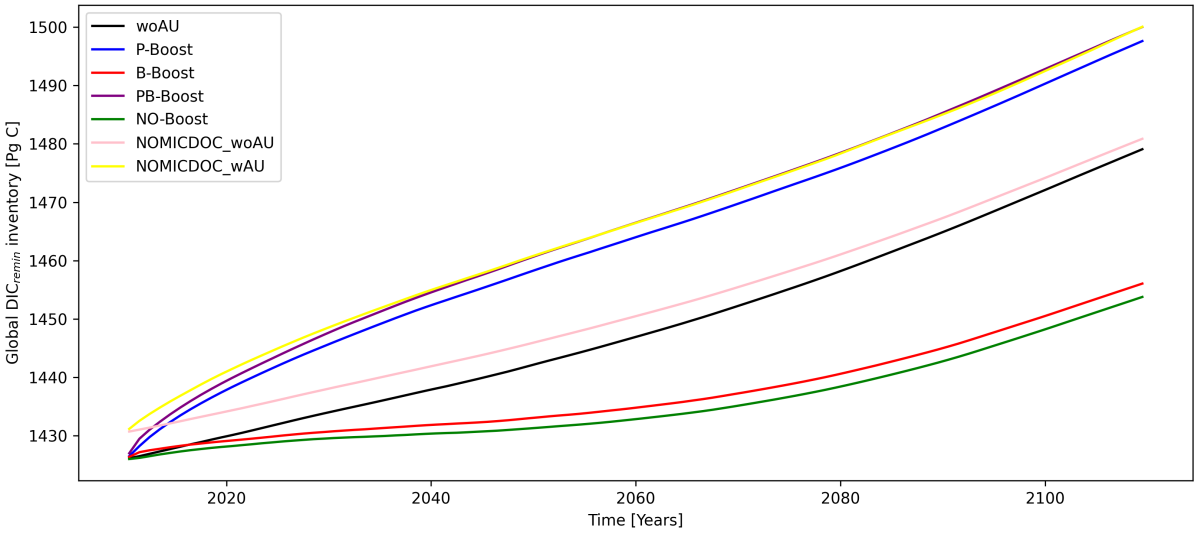


Figure S18: Temporal evolution of the global DIC_{remin} inventory over the 100-year simulation period across all model versions. At each time step, DIC_{remin} was calculated from the oxygen deficit relative to saturation as $\mathrm{DIC}_{remin} = r_{c:o}(O_2 - O_{2,sat})$, where $O_{2,sat}$ is oxygen saturation computed from temperature and salinity, O_2 is modelled dissolved oxygen, and $r_{c:o}$ is the Redfield carbon-to-oxygen stoichiometric ratio. Positive values were integrated over the full ocean volume and converted to Pg C to obtain the global inventory. Differences among simulations corresponds to the color-coded as indicated in the legends.

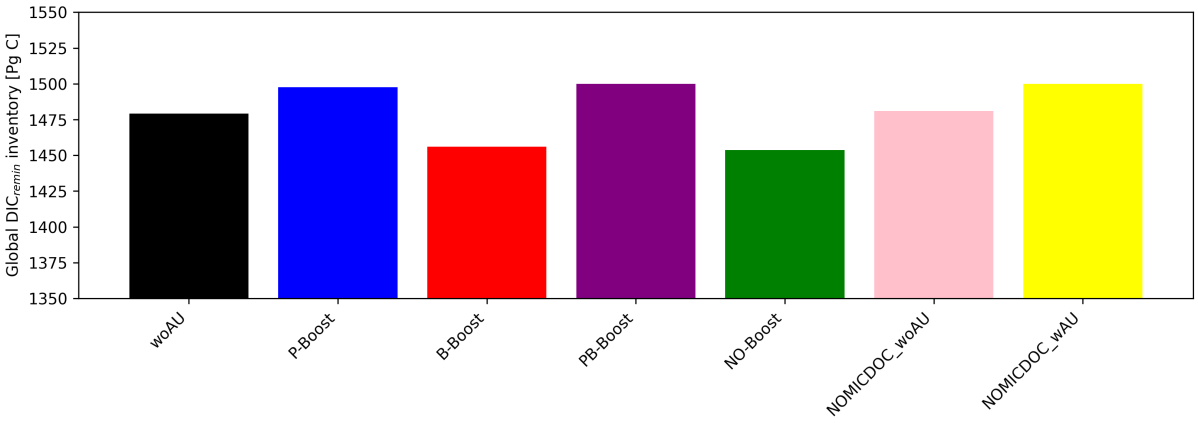


Figure S19: Global inventory of remineralized dissolved inorganic carbon (DIC_{remin}) at the end of the 100-year simulations for all model configurations. DIC_{remin} is calculated from the oxygen deficit relative to saturation as $\mathrm{DIC}_{remin} = r_{c:o}(O_2 - O_{2,sat})$, where $O_{2,sat}$ is oxygen saturation computed from temperature and salinity, O_2 is modelled dissolved oxygen, and $r_{c:o}$ is the Redfield carbon-to-oxygen stoichiometric ratio. Positive values were integrated over the full ocean volume and converted to Pg C to obtain the global inventory. Differences among simulations corresponds to the color-coded as indicated in the legends. The value of $r_{c:o}$ used for the DIC_{remin} calculation is 0.6625 from Frenger et al. (2024).

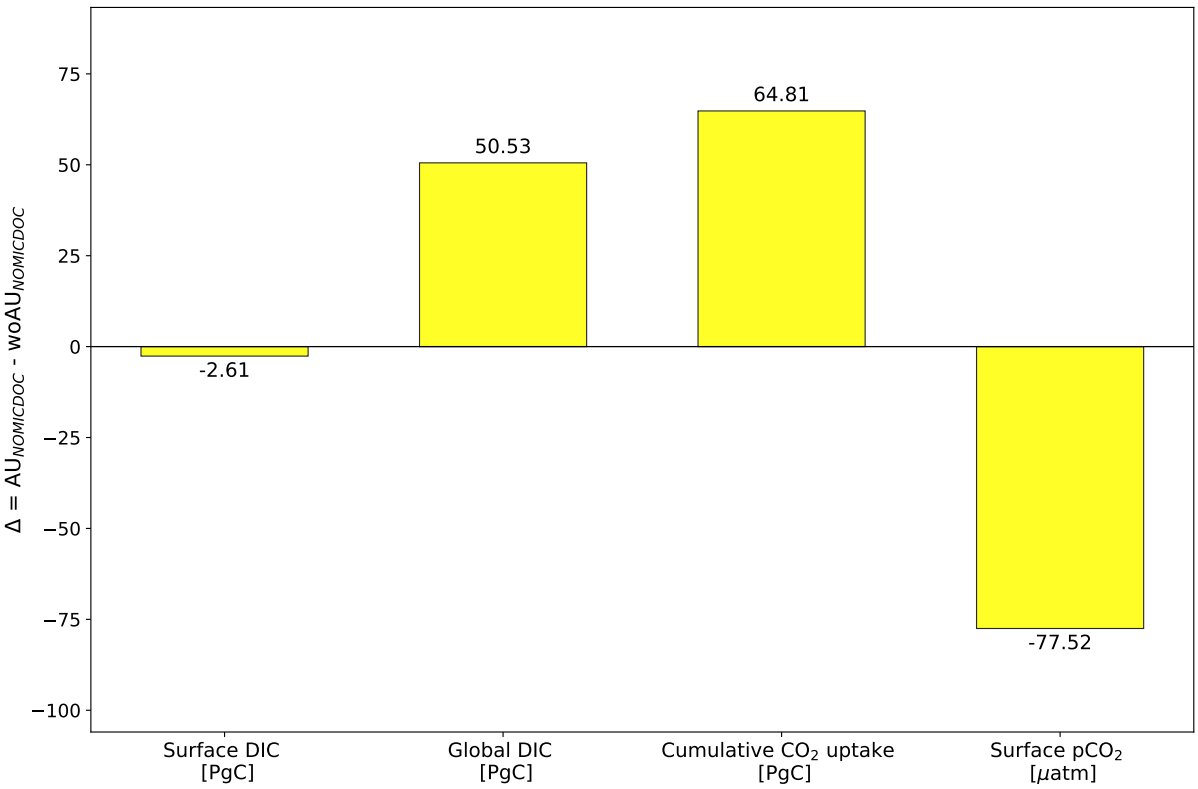


Figure S20: Carbon anomalies associated with AU relative to woAU in the NO-MICDOC simulation, showing surface and global DIC inventories and surface ocean pCO_2 at the end of simulation year 2110, and cumulative air–sea CO_2 uptake over the simulation period.

References

Bitz, C., Holland, M., Weaver, A., and Eby, M. (2001). Simulating the ice-thickness distribution in a coupled climate model. *Journal of Geophysical Research: Oceans*, 106(C2):2441–2463.

Eby, M., Weaver, A. J., Alexander, K., Zickfeld, K., Abe-Ouchi, A., Cimatoribus, A., Crespin, E., Drijfhout, S., Edwards, N., Eliseev, A., et al. (2013). Historical and idealized climate model experiments: an intercomparison of earth system models of intermediate complexity. *Climate of the Past*, 9(3):1111–1140.

Fanning, A. F. and Weaver, A. J. (1996). An atmospheric energy-moisture balance model: Climatology, interpentadal climate change, and coupling to an ocean general circulation model. *Journal of Geophysical Research: Atmospheres*, 101(D10):15111–15128.

Frenger, I., Landolfi, A., Kvale, K., Somes, C. J., Oschlies, A., Yao, W., and Koeve, W. (2024). Misconceptions of the marine biological carbon pump in a changing climate: Thinking outside the "export" box. *Global change biology*, 30(1):e17124.

Galbraith, E. D., Gnanadesikan, A., Dunne, J. P., and Hiscock, M. R. (2010). Regional impacts of iron-light colimitation in a global biogeochemical model. *Biogeosciences*, 7(3):1043–1064.

Garcia, H. E., Weathers, K. W., Paver, C. R., Smolyar, I., Boyer, T. P., Locarnini, M. M., Zweng, M. M., Mishonov, A. V., Baranova, O. K., Seidov, D., and Reagan, J. R. (2019). World ocean atlas 2018. vol. 4: Dissolved inorganic nutrients (phosphate, nitrate and nitrate+nitrite, silicate). Technical report, NOAA Atlas NESDIS 84. A. Mishonov, Technical Editor.

Gent, P. R. and Mcwilliams, J. C. (1990). Isopycnal mixing in ocean circulation models. *Journal of Physical Oceanography*, 20(1):150–155.

Hunke, E. C. and Dukowicz, J. K. (1997). An elastic–viscous–plastic model for sea ice dynamics. *Journal of physical oceanography*, 27(9):1849–1867.

Keller, D. P., Feng, E. Y., and Oschlies, A. (2014). Potential climate engineering effectiveness and side effects during a high carbon dioxide-emission scenario. *Nature communications*, 5(1):3304.

Keller, D. P., Oschlies, A., and Eby, M. (2012). A new marine ecosystem model for the university of victoria earth system climate model. *Geoscientific Model Development*, 5(5):1195–1220.

Locarnini, M. M., Mishonov, A. V., Baranova, O. K., Boyer, T. P., Zweng, M. M., Garcia, H. E., Reagan, J. R., Seidov, D., Weathers, K. W., Paver, C. R., and Smolyar, I. (2018). World Ocean Atlas 2018, Volume 1: Temperature. Technical Report 81, NOAA National Centers for Environmental Information. A. Mishonov, Technical Editor.

Mengis, N., Keller, D. P., MacDougall, A. H., Eby, M., Wright, N., Meissner, K. J., Oschlies, A., Schmittner, A., MacIsaac, A. J., Matthews, H. D., et al. (2020). Evaluation of the university of victoria earth system climate model version 2.10 (uvic escm 2.10). *Geoscientific Model Development*, 13(9):4183–4204.

Orr, J., Najjar, R., Sabine, C., and Joos, F. (1999). Abiotic-howto, internal ocmip report. *LSCE/CEA Saclay*, 25.

Oschlies, A., Pahlow, M., Yool, A., and Matear, R. J. (2010). Climate engineering by artificial ocean upwelling: Channelling the sorcerer's apprentice. *Geophysical Research Letters*, 37(4).

Paulmier, A., Kriest, I., and Oschlies, A. (2009). Stoichiometries of remineralisation and denitrification in global biogeochemical ocean models. *Biogeosciences*, 6(5):923–935.

Schmittner, A., Oschlies, A., Matthews, H. D., and Galbraith, E. D. (2008). Future changes in climate, ocean circulation, ecosystems, and biogeochemical cycling simulated for a business-as-usual co2 emission scenario until year 4000 ad. *Global biogeochemical cycles*, 22(1).

Simmons, H. L., Jayne, S. R., Laurent, L. C. S., and Weaver, A. J. (2004). Tidally driven mixing in a numerical model of the ocean general circulation. *Ocean Modelling*, 6(3-4):245–263.

Tagliabue, A., Bowie, A. R., Boyd, P. W., Buck, K. N., Johnson, K. S., and Saito, M. A. (2017). The integral role of iron in ocean biogeochemistry. *Nature*, 543(7643):51–59.

Wanninkhof, R. (2014). Relationship between wind speed and gas exchange over the ocean revisited. *Limnology and Oceanography: Methods*, 12(6):351–362.

Weaver, A. J., Eby, M., Wiebe, E. C., Bitz, C. M., Duffy, P. B., Ewen, T. L., Fanning, A. F., Holland, M. M., MacFadyen, A., Matthews, H. D., et al. (2001). The uvic earth system climate model: Model description, climatology, and applications to past, present and future climates. *Atmosphere-ocean*, 39(4):361–428.